

## X-RAY $C-M$ RELATION: THEORY AND OBSERVATION

E. RASIA<sup>1</sup>, S. BORGANI<sup>2,3,4</sup>, S. ETTORI<sup>5,6</sup>, P. MAZZOTTA<sup>7,8</sup>, M. MENEGHETTI<sup>5,6</sup>

<sup>1</sup> Department of Physics, University of Michigan, 450 Church St., Ann Arbor, MI 48109

<sup>2</sup> Dipartimento di Fisica dell' Università di Trieste, Sezione di Astronomia, via Tiepolo 11, I-34131 Trieste, Italy

<sup>3</sup> INAF, Osservatorio Astronomico di Trieste, via Tiepolo 11, I-34131, Trieste, Italy

<sup>4</sup> INFN, Istituto Nazionale di Fisica Nucleare, Trieste, Italy

<sup>5</sup> INAF, Osservatorio Astronomico di Bologna, v. Ranzani 1, I-40127, Bologna, Italy

<sup>6</sup> INFN, Sezione di Bologna, viale Berti Pichat 6/2, I-40127, Bologna, Italy

<sup>7</sup> Dipartimento di Fisica, Università di Roma Tor Vergata, via della Ricerca Scientifica, I-00133, Roma, Italy

<sup>8</sup> Harvard-Smithsonian Center for Astrophysics, 60 Gardner Street, Cambridge, MA 02138, USA

*Draft version July 19, 2022*

### ABSTRACT

Since fifteen years, the concentration-mass relation has been investigated diffusely in theoretical studies. On the other hand, only recently this relation has been derived from X-ray observations. When that happened, the results caused a certain level of concern: the X-ray normalizations and slopes were found significantly dissimilar from those predicted by theory.

By analyzing a total of 52 objects, simulated each time with different physical recipes for the baryonic component, as well as 60 synthetic X-ray images, we aim at determining if these discrepancies are real or artificial. In particular, we investigate how the simulated concentration-mass relation depends *i*) on the radial range used to derive the concentration, *ii*) on the presence of baryons in the simulations, and on the prescription used to reproduce the gas. Finally, we evaluate *iii*) how the results differ when adopting an X-ray approach for the analysis and *iv*) how the selection functions based on X-ray luminosity, temperature, and SZ-signal can impact the results. All effects studied go in the direction of explaining the discrepancy between observations and simulations, but they contribute at different levels: while the fitting radial range and the baryonic component play only a minor role, the X-ray approach and selection function have profound repercussion on the results.

Extending the fit to the most central regions or reducing the fitting radius from the virial boundary to the typical X-ray external radius causes an increase of the normalization. In the second case, a steeper slope is also found. Modifications in normalization or slope are more acute when baryons are included. Radiative simulations with only SN feedback present 30% higher concentrations than the DM case. The discrepancy is cancelled when the more powerful feedback by AGNs is considered. The concentration-mass relation derived from the X-ray synthetic catalogue is significantly steeper because the simultaneous influence of multiple effects such as environment, dynamical state, dynamical history, mass bias, temperature bias, and their dependences on the radius and on the mass of the system. Finally, selecting the system via their SZ signal or mass-weighted temperature does not create any extra bias while a X-ray luminosity-based choice produces a net steepening of the relation since in the group-regime the most luminous systems are also the most concentrated.

*Subject headings:* clusters: general — clusters: ICM — clusters: cosmology — X-rays: clusters

### 1. INTRODUCTION

The dark sector (dark energy and dark matter - DM) exceeds by about twenty-five times the baryonic content of our Universe (e.g. Voit 2005; Borgani & Kravtsov 2011; Allen et al. 2011 for recent reviews on cosmology with focus on galaxy clusters). As consequence, at first approximation, we may assume that simulations with only dark components properly describe the salient halo properties such as the mass distribution, the tridimensional halo shape, the density profile, and the concentration (see Kravtsov & Borgani 2012, for a galaxy-cluster-formation review). However, an increasing number of theoretical papers begun to contest this simplistic view showing that baryons (in form of both hot gas and stars) can significantly influence all these topics (e.g. Rudd et al. 2008; Stanek et al. 2009; Duffy et al. 2010; Cui et al. 2012; Lau et al. 2011; Gnedin et al. 2011; van Daalen et al. 2011; Zhu & Pan 2012; Macciò et al. 2012; Governato et al. 2012; Balaguera-Antolinez & Porciani 2012, among the most recent publications on the various aspects). Some disagreement between some observational results and theoretical predictions based on DM-only simulations support this discomfort. In this respect, a recent debate

about the X-ray observed and simulated concentration-mass relation warmed up (Fedeli 2012, and references therein). Indeed, while earlier works based on 10-12 clusters observed by *Chandra* (Vikhlinin et al. 2006) and *XMM-Newton* (Pratt & Arnaud 2005; Pointecouteau et al. 2005) showed consistency with theoretical works (Dolag et al. 2004), lately, with the enlargement of the observational collections, more differences have arisen. The concentration-mass relation from the larger X-ray samples of Buote et al. (2007, B07), Schmidt & Allen (2007, SA07), and Ettori et al. (2010, E10) are significantly steeper (Fedeli 2012) than the relation derived from the Millenium simulation (Gao et al. 2008, with results similar to aforementioned work by Dolag et al. 2004). An exception to this mismatch is the result by Host & Hansen (2011) who, however, analyzed only 11 systems.

The question we want to answer in this paper is *whether the differences between theory and observations are real* – i.e. some fundamental physical ingredients are missing in theoretical models – *or artificial* – i.e. the comparison is conducted in an unfair fashion without considering possible biases that depend on the methods employed.

All the mentioned papers on the c-M relations consistently

adopt the Navarro-Frenk-White (NFW) analytic model to fit the density profile and derive the concentration. Navarro et al. (1996) showed the existence of an universal profile that well describes the halo density and mass distribution for a large range of halo mass and cosmologies (Navarro et al. 1997). Their fitting formulae are characterized by two parameters: the normalization,  $\rho_s$ , and the scale radius,  $r_s$ . The expressions for the profiles of the NFW density and the NFW mass, as function of  $x = r/r_s$ , are respectively:

$$\rho(x) = \frac{\rho_s}{x(1+x)^2}, \quad (1)$$

$$M(<x) = 4\pi\rho_s r_s^3 f_x, \quad f_x = \ln(1+x) - x/(1+x). \quad (2)$$

The logarithmic slope of the density profile measured at the scale radius is equal to  $-2$ , transitioning from the central asymptotic value of  $-1$  to the external value of  $-3$ . The normalization factor,  $\rho_s$ , is connected to the characteristic overdensity,  $\Delta$ , and to the critical density at the halo redshift  $z$ ,  $\rho_{cr}$ , through:

$$\rho_s = \frac{\Delta\rho_{cr}}{3} \frac{c^3}{\ln(1+c) - c/(1+c)} \quad (3)$$

where the critical density can be expressed as  $\rho_{cr} = 3H^2(z)/(8G)$ , with  $H(z)$  the Hubble's parameter at redshift  $z$  and  $G$  the Newton's gravitational constant. Finally,  $c$  is the concentration of the halo and it is defined as the number of times the scale radius is contained within a fixed overdensity radius:  $c = R_\Delta/r_s$ . In the following, we will always define the concentration in relation to the overdensity  $\Delta = 200^1$ .

The origins of the density shape mostly resides on the density and triaxiality of the original peak and on the continuous contraction of the innermost material due to subsequent accretion during the collapse (Dalal et al. 2010). This last point is also a suitable explanation for the increase of the concentration parameter with the decrease of mass (e.g., NFW, Eke et al. 2001; Bullock et al. 2001; Dolag et al. 2004; Zhao et al. 2009). The physical and cosmological justification is linked to the hierarchical scenario of structure formation: small halos form at earlier time when the universe was denser than today and, over time, the sedimentation of material at the center happens in an already-established high-density peak.

The measure of a negative slope from observations is, therefore, expected. The surprise is related to the values: the X-ray slope is up to 5 times steeper than what found in DM cosmological simulations. In this paper, we want to test if this result is produced by hidden biases related to the two methods followed to analyze simulated and observed data. Indeed, it is unquestionable that the basic procedural assumptions of the two analyses differ in several aspects. The *simulated concentration-mass relation* is mostly derived by fitting the NFW profile to the three-dimensional density distribution extracted considering the influence of all the particles without exclusion of sub-structures or sub-clumps, and from the really central region to the outskirts of the halo, usually up to the virial region, sometimes beyond. The sample selection is typically volume-limited with a well defined cut in mass. Finally, as said above, many theoretical works are based on large cosmological boxes of DM only (e.g. Bhattacharya et al. 2011; Kwan et al. 2012, among the most recent ones). On the contrary, the *X-ray concentration-mass relation* is derived from projected data that have a limited radial range because of the signal-to-noise and the field of view.

Few clusters have been observed to  $R_{500}$  with enough photon statistics and even fewer at  $R_{200}$ . For example, E10 (one of the samples we are comparing to) reaches on average 40% of  $R_{200}$  (see Section 3.3.1). The observational selection function is not done in mass. In the best case, depends on the X-ray luminosity. In the worse (and the most common) situation, the clusters are chosen among the ones available on the archives, as consequence the selection function is not well defined. As final note, the real universe has baryons.

The possibility that baryons might influence the structure-formation process and, in particular the DM distribution, has been introduced almost three decades ago with the development of the analytic model of ‘adiabatic contraction’ (Barnes & White 1984; Blumenthal et al. 1986; Ryden & Gunn 1987). More recently cosmological simulations push further the improvement of the model (e.g. Gnedin et al. 2004; Gustafsson et al. 2006; Abadi et al. 2010; Tissera et al. 2010; Gnedin et al. 2011; Zemp et al. 2012). The underlying idea is that, at the center, the DM feels the growth of the total potential well due to the extra baryonic material accreted in consequence of cooling and condensation. However, even if a specific great effort has been devoted to study the concentration parameter in non-radiative simulations (e.g. Rasia et al. 2004; Pedrosa et al. 2009; Tissera et al. 2010) only recently these investigations have been extended to include various model of the intra-cluster medium (ICM) (Rudd et al. 2008; Duffy et al. 2010; Meneghetti et al. 2010; Macciò et al. 2012; Governato et al. 2012; Martizzi et al. 2012; Ragone-Figueroa et al. 2012) and also different dark-energy models (Grossi & Springel 2009; Baldi 2012; De Boni et al. 2013).

Summarizing, we aim at evaluating how the different steps and assumptions behind the two analyses can explain the dissimilar findings on the simulated and the X-ray-observed  $c-M$  relations. In particular we focus on the impact of *i)* the radial range, *ii)* the presence of baryons, *iii)* the X-ray analysis, and *iv)* the choice of the selection function. To reach these goals, we perform an intrinsic analysis on four sets of 52 clusters simulated each time with a different recipe for the ICM (runs include increasing level of complexity: DM only run, no-radiative ICM, cooling and feedback by mainly supernovae Ia and II, feedback by mainly active galactic nuclei). Finally, we follow an X-ray approach on the synthetic Chandra-like catalogue introduced by Rasia et al. (2012a,b, R12)<sup>2</sup>.

Let us restate and stress that the goal of the paper is not to provide another prediction for the  $c-M$  relations or to tackle the long-standing ‘cusp-versus-core debate’ (e.g. Ogiya & Mori 2011; Macciò et al. 2012; Teyssier et al. 2013; Martizzi et al. 2012) or the problem of the goodness of the NFW to describe density profiles of galaxy clusters (Meneghetti & Rasia, 2013). For these purposes, the size of our sample, even if comparable to observational works, is too small. We intend, instead, to check all procedural steps that can convey *systematic biases affecting the  $c-M$  relation*. We will discuss further the limits of our sample and possible influence on the results obtained.

This paper is organized as follows: after presenting the simulations in Section 2, we discuss the results derived from the intrinsic analysis of the simulated clusters in Section 3. The observational approach applied to synthetic X-ray images will

<sup>1</sup>  $R_{200}$  is the radius of the sphere enclosing a mean density 200 times the critical density. Conversions of the NFW mass defined for different values of  $\Delta$  are provided in the Appendix of Hu & Kravtsov (2003) and Appendix of Ettori et al. (2010).

<sup>2</sup> A video abstract of R12 (Rasia et al. 2012b) can be found at the following link: <http://iopscience.iop.org/1367-2630/14/5/055018?fromSearchPage=true>. The images of the synthetic catalogue can be found at <http://www-personal.umich.edu/~rasia/>

be presented in Section 4, while in Section 5 we will focus on the choice of the selection function. Our conclusions are outlined in Section 6.

## 2. SIMULATIONS

In this Section, we briefly describe the four sets of simulated clusters that are used in our intrinsic analysis (Section 3). These four sets are obtained starting from the same initial conditions and using four different physical descriptions of the processes determining the evolution of the baryonic component. More details on the generation of the initial conditions are provided by Bonafede et al. (2011), while we refer to Killevar et al. (2012) for a description of the different physical models implemented, and to Rasia et al. (2012a,b) for the characterization of the synthetic X-ray catalogue of X-ray.

### 2.1. The sets of simulated clusters

Our simulated clusters have been chosen within twenty nine Lagrangian regions identified within a  $1\text{ h}^{-3}\text{Gpc}^3$  low-resolution N-body cosmological simulation<sup>3</sup>. The cosmological model assumed is a flat  $\Lambda$ CDM model, with  $\Omega_m = 0.24$  for the matter density parameter,  $\Omega_{\text{bar}} = 0.04$  for the contribution of baryons,  $H_0 = 72\text{ km s}^{-1}\text{Mpc}^{-1}$  for the present-day Hubble constant,  $n_s = 0.96$  for the primordial spectral index and  $\sigma_8 = 0.8$  for the normalization of the power spectrum. Resolution is increased within the selected regions by enlarging the number of particles and correspondingly adding higher-frequency modes from the power spectrum of the same cosmological model, by using the Zoomed Initial Condition (ZIC) technique (Tormen et al. 1997). The runs were carried out using the GADGET-3 code, a newer and more efficient version of the former GADGET-2 code (Springel 2005). In all simulations a Plummer-equivalent softening length for the computation of the gravitational force in the high-resolution region was fixed to  $\epsilon = 5\text{ h}^{-1}\text{kpc}$  in physical units for most recent redshift ( $z < 2$ ), while was kept fixed in comoving units at earlier epochs. As for the computation of hydrodynamic forces, we assume the SPH smoothing length to reach a minimum allowed value of  $0.5\epsilon$ .

Besides a set of dark matter only (DM) simulations and a set of non-radiative (NR) hydrodynamical simulations, we also carried out two sets of radiative simulations (CSF and AGN). In these simulations radiative cooling rates are computed by following the procedure presented by Wiersma et al. (2009), including the effect of CMB radiation and of UV/X-ray background radiation from quasars and galaxies (Haardt & Madau 2001). The contributions to cooling from eleven elements (H, He, C, N, O, Ne, Mg, Si, S, Ca, Fe) have been pre-computed using CLOUDY (Ferland et al. 1998) for an optically thin gas in (photo-)ionisation equilibrium.

The CSF set of simulations includes star formation and the effect of feedback triggered by supernova (SN) explosions. As for the star formation model, gas particles above a given threshold density are treated as multiphase, so as to provide a sub-resolution description of the interstellar medium, according to the model originally described by Springel & Hernquist (2003). SN-II, SN-Ia and low and intermediate mass stars contribute to the production of metals according to the model described by Tornatore et al. (2007): assuming a Chabrier IMF (Chabrier 2003) stars produce metals over the time-scale determined by the mass-dependent life-times of Padovani & Matteucci (1993).

The effect of kinetic feedback triggered by SN-II is included according to the prescription by Springel & Hernquist (2003). In the CSF simulation set we assume  $v_w = 500\text{ km s}^{-1}$  for the velocity of the outflows, with a mass-upload rate that is two times the value of the local star formation rate.

The AGN set of simulations is carried out by including the same physical processes as in the CSF case, with a lower wind velocity of  $v_w = 350\text{ km s}^{-1}$ , but also including the effect of AGN feedback. In this model, largely based on the original implementation of black-hole (BH) feedback by Springel et al. (2005), energy results from gas accretion onto supermassive black holes. BHs are included as sink particles, which grow in mass by gas accretion and merging with other BHs. Gas accretion proceeds at a Bondi rate, and is limited by the Eddington rate. Once the accretion rate is computed for each BH particle, a stochastic criterion is used to select the surrounding gas particles to be accreted. Unlike in Springel et al. 2005, in which a selected gas particle contributes to accretion with all its mass, we included the possibility for a gas particle to accrete only with a slice of its mass, which corresponds to 1/4 of its original mass, thus providing a more continuous description of the accretion process (see also Fabjan et al. 2010). BH particles are initially seeded with a mass of  $5 \times 10^8\text{ h}^{-1}\text{M}_\odot$ . Seeding of BH particles takes place at the minimum of the potential of halos when they first reach a minimum friend-of-friend mass of  $2.5 \times 10^{13}\text{ h}^{-1}\text{M}_\odot$  (using a linking length of 0.16 in units of the mean interparticle separation), with the further condition that such halos should contain a minimum mass fraction in stars of 0.02. This condition guarantees that substantial star formation took place in such halos and that seeding does not take place in structures linked together by the friend-of-friend algorithm, not corresponding to a real halo. A radiation efficiency parameter of  $\epsilon_r = 0.1$  determines the amount of radiated energy extracted from gas accretion, in units of the rest-mass energy of the accreted gas, with the BH mass being correspondingly decreased by this amount. A fraction  $\epsilon_f$  of this radiated energy is thermally coupled to the surrounding gas. We use  $\epsilon_f = 0.05$  for this feedback efficiency, which increases to  $\epsilon_f = 0.2$  when accretion enters in the quiescent “radio” mode and takes place at a rate smaller than one-hundredth of the Eddington limit (e.g. Sijacki et al. 2007; Fabjan et al. 2010).

The analysis described in Section 3 is based on a sample of 52 objects. These are the central clusters of each of the 29 region plus three halos selected from rich environment (regions containing more than 20 halos with virial mass greater than  $5 \times 10^{13}\text{ h}^{-1}\text{M}_\odot$ ), six from poor environment (less than 8 halos per region in the same mass limit), and fourteen lying in a medium populated environment. The covered mass interval is similar to that usually considered in observational works, with  $M_{200}$  ranging from  $7.5 \times 10^{13}\text{ h}^{-1}\text{M}_\odot$  to  $2.5 \times 10^{15}\text{ h}^{-1}\text{M}_\odot$ . All clusters have been analyzed at redshift zero (for comparison with other works present in literature) and 0.25 (for comparison with the X-ray sample of R12). Throughout the paper, we will focus on the  $z = 0$  objects reporting our  $z = 0.25$  results in the Appendix.

### 2.2. Synthetic catalogue

The X-ray synthetic catalogue employed in Section 5 and 6 contains 60 event files related to three orthogonal projections of twenty massive objects part of the CSF sample at  $z = 0.25$ .

The X-ray catalogue has been created using the *X-ray MAP Simulator* (X-MAS Gardini et al. 2004; Rasia et al. 2008) after

<sup>3</sup>  $h = 0.72$  throughout the paper

the removal of the over-cooled particles identified in the density ( $\rho[\text{gr}/\text{cm}^3]$ ) – temperature ( $T[\text{keV}]$ ) plane that satisfy to the condition:  $T < 3 \times 10^6 \rho^{0.25}$ . This cut reduces the presence of small peaked clumps in the X-ray images without affecting the overall distributions of density, temperature, and X-ray luminosity (see Appendix of R12). The redistribution matrix function and ancillary response function adopted are those of *Chandra* ACIS-S3. The field of view is 16 arcmin, equivalent to  $\sim 2.5$  Mpc for our cosmology and redshift, and the exposure time is of 100 ksec. The metallicity is kept constant to 0.3 solar with respect to the tables of Anders & Grevesse (1989) with a small correction on the helium abundances to be consistent with the simulated hydrogen mass fraction. The galactic absorption, described by a *WABS* model, is fixed to  $N_H = 5 \times 10^{-20} \text{ cm}^{-2}$ . Along the line of sight, we consider the information of all the particles located up to  $5 \text{ h}^{-1} \text{ Mpc}$  (in both directions) from the center of the object. The final event files avoid the inclusion of the background since this component does not influence the mass profile derivation (Rasia et al. 2006, 2012b).

### 3. INTRINSIC C-M

#### 3.1. Density profiles and fitting procedure

To perform the tri-dimensional analysis of our simulated sample, we proceed by extracting the spherical mass profiles in 50 bins logarithmically spaced from  $10 \text{ h}^{-1} \text{ kpc}$  to  $5 \text{ h}^{-1} \text{ Mpc}$  and centered on the minimum of the potential well. For each cluster, all the bins external to  $\approx 2\%$  of  $R_{200}$  have more than one thousand particles. This number represents the threshold for numerical convergency of the inner slope (Power et al. 2003). Following the observational approach, we fit our simulated profile with the NFW mass expression (Eq. 2) to recover the two parameters  $\rho_s$  and  $r_s$ . The process is performed multiple times on the same object changing in each circumstance the radial range assumed (Section 3.3.1). As subsequent step, we derive the NFW concentration using Eq. 3. The concentration-mass relation is, then, calculated by linearly fitting the following expression:

$$\log_{10} c = \log_{10} c_0 + \alpha \times \log_{10} \frac{M_{\text{NFW}}}{5 \times 10^{14} \text{ h}^{-1} \text{ M}_{\odot}} \quad (4)$$

For the hydro-simulations (NR, CSF, and AGN), we analyze both the total mass profile and the profile of the only dark matter. In each radial bin, the NFW fitting procedure assumes an error on the mass equivalent to 10% of the mass itself, value consistent with observations and previous analyses on X-ray synthetic catalogues (Meneghetti et al. 2010, R12).

#### 3.2. Redefinition of the sample

When studying the influence of the radial range (Section 3.3) and the baryonic physics (Section 3.4), we consider *only* the profiles that show a good consistency with the NFW description. In this way we exclude both objects that presenting one or more large substructures produce a secondary peak in the density profile and halos that do not have a coherent concentration parameter associated. This *a priori*-selection is not usually embraced in theoretical works, however, it is often implicitly adopted in observational samples especially if they are focused on regular systems. The careful choice of the simulated clusters that need to be discarded is done on the basis of the NFW residuals:

$$\sigma^2 = \frac{\sum_i^{N_{\text{bin}}} [\log_{10}(M_i) - \log_{10}(M_{\text{NFW},i})]^2}{N_{\text{bin}}} \quad (5)$$

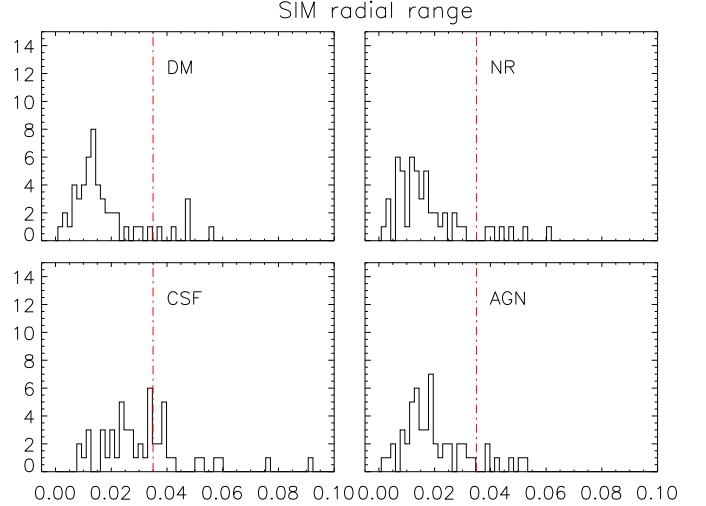


FIG. 1.— Distribution of residuals as defined in Eq.5 of the four physics and at redshift zero. The concentration is derived assuming the SIM radial range,  $[0.06 - 1.27] \times R_{200}$ , as defined in Section 3.3.1. Acceptable clusters have residuals below 0.035 (red dotted vertical line).

For all situations considered (varying ICM physics or radial ranges) and for both redshifts, we study the distributions of the residuals and notice that the majority of the objects has residuals below 0.035 at  $z = 0$  (see Figure 1) and 0.05 at  $z = 0.25$ . The residuals are significantly larger at  $z = 0.25$  especially for the NR physics. Furthermore, at fixed redshift, the outliers are often the same objects despite the change of the simulated set or the fitting radial range. Per each redshift, we identify these systems: nine clusters at  $z = 0$  and eleven at  $z = 0.25$ . The NR physics presents larger deviations because accreted substructures requires more time to virialize and thermalize under the no-radiative physical condition (Dolag et al. 2009).

In the following, we decide to always exclude these identified systems and any other existing outliers (defined as having  $\sigma > 0.035$  at  $z = 0$  and  $\sigma > 0.05$  at  $z = 0.25$ ). For each situation investigated, before deriving the  $c-M$  relation, we check whether the excluded halos are spread across the mass range. When this does not happen (for example, if all object below a certain mass disappear) we prefer to not show the derived  $c-M$  relation because of the significant change on the statistical conditions.

### 3.3. Radial range

#### 3.3.1. Typical theoretical and observational radial range

Previous works demonstrated that the fitting radial range has some level of impact on the derived NFW concentration. For example, Rasia et al. (2006) showed that the concentration of a single clusters varies from  $\sim 5.3$  to 7 (23% variation) when the outer radius moves from the virial radius to 20-30% of that radius. Using their X-ray observations on A2717, Gastaldello et al. (2007) warned on the derivation of the concentration parameter if the data do not extend beyond the measured scale radius. Fedeli (2012) stressed more on the consequences of the choice of the inner radius: fitting from 1% of  $R_{200}$  induces an higher concentration, especially in small systems, than starting from 5% of  $R_{200}$ .

To evaluate the influence of the radial range assumed to fit the mass profile with the NFW formula, we begin by studying the DM sample. We first consider radial ranges that are ‘typi-

cally’ used in theory and X-ray studies, then we move to a more general discussion.

Our reference for theoretical works are Neto et al. (2007), Duffy et al. (2008, 2010) and Meneghetti & Rasia (2013). Their radial range used to fit the NFW formula is between 5% and 100% of the virial radius. The innermost limit was set to satisfy the requirement on the numerical convergence (Section 3.1 and Power et al. 2003). As done by most observational works, we prefer to report all the measurements to  $R_{200}$ , that is equal to  $R_{\text{vir}}/1.27$  for our sample, redshifts, and cosmology. Therefore, the typical simulation radial range is  $[0.06, 1.27] \times R_{200}$ . We label this radial range as SIM.

The X-ray radial range is, instead, linked to the one used in Ettori et al. (2010). The Authors provided the radial boundaries used to compute the NFW best fit. The inner radius was constantly fixed to 50 kpc to exclude the impact of the central galaxy on the density profile and thus avoiding the stellar component influence. In our whole sample, this value is larger than  $0.03 \times R_{200}$  fulfilling the convergency requirement. E10 also furnished two outer radii, one associated to the surface brightness profile and the other to the spectroscopic temperature profile. Per each cluster, we select the minimum of the two and compare its values to the derived  $R_{500}$ . The mean ratio resulted to be equal to  $0.6^4$ . Concluding, we label the radial range from 50 kpc to  $0.6 \times R_{500}^5$  as X-RAY.

Considering both the SIM and the X-RAY radial ranges we fit the same DM cluster mass profiles, derive values of both NFW concentration and mass, and fit the concentration-mass relation with Eq. 4. For the  $z=0$  sample the resulting normalization,  $c_0$ , and slope,  $\alpha$ , are reported in the first two rows of the first section of Table 1 with their  $1\sigma$  error. The two slopes are consistent within  $1\sigma$  while the normalization, when a typical X-RAY radial range is used, increases by 6-10% with respect to the theoretical radial range. Limiting the fit to inner parts of the mass profile produces an increase of the halo concentration at all mass scale. The cause is the combined effects of lowering both the internal and external boundaries. In this circumstance, the innermost part of the profile weights very strongly. Indeed, within  $100 h^{-1}$  kpc almost all the NFW X-RAY best fits are lying above the SIM ones. Comparing the concentrations, the scale radii, and the two  $R_{200}$  derived, we found that with respect to the SIM radial range: *i*) the X-RAY  $R_{200}(=r_s \times c)$  is only 4% lower; *ii*) the X-RAY scale radii are significantly lower ( $\sim 13\%$ ) and, consequently, *iii*) the X-RAY concentrations are higher ( $\sim 16\%$ ).

### 3.3.2. Radial range generalization

To broaden the discussion about the radial ranges, we explore some variation on the external and the internal radii with respect to the SIM radial range. The results are shown in Figure 2 and listed in Table 1. For clarity, we show the cluster points only for the SIM radial range. In the top panel, the inner radius is constantly equal to  $0.06 \times R_{200}$  while the external one varies from  $0.4 \times R_{200}$  (solid blue line) to  $2 \times R_{200}$  (dashed orange line). From this plot, it appears that both slopes and normalization slightly increase when the external radius becomes smaller and closer to the X-RAY limit ( $0.6 \times R_{500} \sim 0.4 \times R_{200}$ ).

Even if the changes are very small and within  $1\sigma$ , we tested

<sup>4</sup> In Ettori et al. (2010) two different  $R_{500}$  radii were reported accordingly to two different derivations of the mass profiles. For our purpose, the variation between these are minimal, as we tested.

<sup>5</sup> this value corresponds roughly to  $0.4 \times R_{200}$  for our objects.

TABLE 1

CONCENTRATION-MASS BEST-FIT PARAMETERS WITH  $1\sigma$  ERROR OF THE DM SAMPLE AT REDSHIFT  $z=0$ . APART THE X-RAY RADIAL RANGE FIXED BETWEEN 50 KPC AND  $0.6 \times R_{500}$ , ALL REMAINING RADIAL RANGES ARE DEFINED IN UNITS OF  $R_{200}$ , WITH  $\text{SIM}=[0.06-1.27] \times R_{200}$ .

fitting radial range	N	DM $\alpha$	$c_0$
SIM	43	$-0.156 \pm 0.033$	$3.724 \pm 0.015$
X-RAY	42	$-0.114 \pm 0.034$	$4.014 \pm 0.015$
[0.06–0.4]	43	$-0.153 \pm 0.034$	$3.844 \pm 0.016$
[0.06–2.0]	43	$-0.137 \pm 0.033$	$3.722 \pm 0.015$
[0.03–1.27]	42	$-0.123 \pm 0.032$	$3.827 \pm 0.015$
[0.2–1.27]	43	$-0.142 \pm 0.037$	$3.597 \pm 0.017$

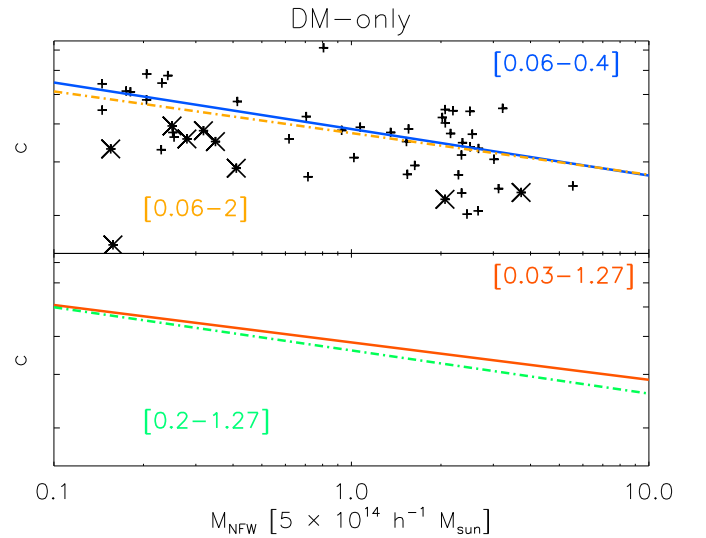


FIG. 2.— Each line represent a different concentration mass-relation extracted by varying the limits of the SIM radial range. In the top panel, we vary the external radius from 0.4 (solid blue line) to  $2 \times R_{200}$  (dotted-dashed orange line). In the bottom panel, the internal radius moves from 0.03 (solid red line) to  $0.2 \times R_{200}$  (dotted-dashed green line). The points are the values of NFW concentrations and masses computed assuming the SIM radial range. The big crosses indicate the 9 clusters excluded for their large residuals.

the origin of this trend. We found that halos with different masses react differently to changes of the radial fitting: smaller halos play the major role. For example, the parameters  $\rho_s$  and  $r_s$ , of our most massive clusters ( $M_{\text{true}} > 10^{15} h^{-1} M_{\odot}$ )<sup>6</sup> do not depend on the radial range chosen implying an averaged small variation on the NFW masses and concentrations ( $< 5\%$ ). The largest contributors of the slope variation are objects with low mass. Our smallest clusters ( $M_{\text{true}} < 1.5 \times 10^{14} h^{-1} M_{\odot}$ ) show a change in the scaling radius and in the normalization of  $\sim 20\%$  and  $\sim 25\%$  when moving from the widest ( $[0.06-2] \times R_{200}$ ) to the narrowest ( $[0.06-0.4] \times R_{200}$ ) radial range. The consequence is to produce a  $\sim 10\%$  larger concentration and  $20\%$  smaller NFW mass with a shift not parallel to the SIM concentration-mass relation but almost orthogonal to it causing the overall change of the slope. We conclude that the radial range might play a more relevant role whenever the sample extends to small

<sup>6</sup> We indicate with  $M_{\text{true}}$  the true mass of the simulated objects within  $R_{200}$ . Notice that it might differ from the NFW masses reported in the various Figures.



halos.

The other scenario presented in the lower panel of the same Figure 2 regards the change on the inner radius from  $0.03 \times R_{200}$  (dotted-dashed red line) to  $0.2 \times R_{200}$  (solid green line) while the external radius is kept fixed at  $1.27 \times R_{200}$ . Excluding a significant portion of the inner profile (with a cut similar to that applied in weak-lensing studies) causes a reduction on the normalization. Vice versa, extending the fit to inner regions (i.e. to values comparable to the X-RAY inner radius) increases the normalizations as previously noticed comparing the X-RAY and SIM radial ranges. Also in this case, however, the modifications in the concentration-mass relation are not enough to explain the differences between the simulated and observed relations.

### 3.4. Impact of baryons: $c$ - $M$ relation

To evaluate the influence of baryons and of the baryonic physics on the  $c$ - $M$  relation, we fit the NFW formula (Eq. 2) to the mass profiles of the hydro simulations using all the radial ranges discussed above (SIM, X-RAY, and the four cases of Figure 2 and Table 1). On top of the total mass profile, in this Section, we have considered also the DM-only mass profile, i.e. the mass profiles derived from the DM particles within the hydro-simulations (thus, ignoring both baryonic components: gas and star).

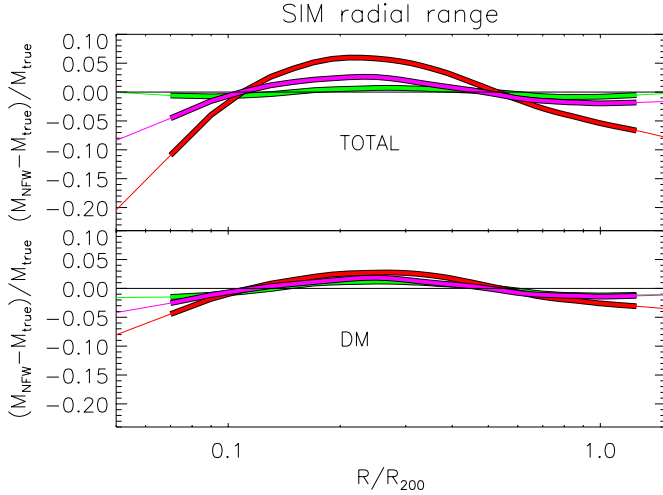


FIG. 3.— Profiles of the residuals for all the hydro simulation (NR in green, CSF in red, and AGN in magenta) at redshift zero. The NFW fitting is derived assuming the SIM radial range  $([0.06 - 1.27] \times R_{200})$  as defined in Section 3.3.1). In the top panel, the NFW fit is applied to the total mass profile, while in the bottom one to the mass profiles of the DM-particles.

#### 3.4.1. Deviation from the NFW formula

The number of clusters whose mass profiles are well fitted by the NFW formalism (see Section 3.1) is also listed in the same Table. The CSF sample is heavily reduced due to large deviation from the NFW formula especially at small radii. This is evident looking at the top panel of Figure 3 where we show the average profiles of the NFW-mass deviations from the true mass profile:  $(M_{\text{NFW}} - M_{\text{true}})/M_{\text{true}}$ . The Figure built excluding the nine systems with large residuals (see Section 3.1). Even so, the CSF clusters (in red) largely depart from a pure NFW at the center. The NR clusters (in green) are very well represented by the NFW formula showing almost zero deviations at all radii. The AGN runs are halfway. Since they include radiative cooling,

as the CSF runs, they also have central profiles steeper than an NFW profile and than the NR clusters. However, the presence of AGNs, which push a considerable amount of gas towards more external radii, reduces this effect with respect to the CSF simulations (Fabjan et al. 2010).

The condensation of baryons in the center is very efficient in less massive objects. Indeed, almost all our CSF groups with  $M_{\text{true}} < 2 \times 10^{14} h^{-1} M_{\odot}$  have residuals  $\sigma > 0.035$  when the fit is extended to a small innermost limits such as either  $0.03 \times R_{200}$  or 50 kpc. The exclusion of all these systems implies a drastic reduction of the mass range impeding to robustly derive the  $c$ - $M$  relation.

From the bottom panel of Figure 3, we learn that the NFW is an excellent description of the mass profiles of the DM-only particles. Looking at similar profiles generated by varying the radial range adopted (not shown), we notice that this feature persists at all times. As further confirmation, when we restrict our analysis to the dark component only few objects show large residuals. Indeed, in Table 2, the values of  $N$  associated to the DM mass profiles within the hydro-simulations are almost always equal to 43.

#### 3.4.2. Comparison with the DM set: slope

The results of the baryonic simulations, presented in Table 2, indicate that the slopes of the  $c$ - $M$  relations are always consistent within  $1 \sigma$  error with the DM slopes (Table 1). However, when baryons are included we see an amplification of the effects discussed in Section 3.3. For example, enlarging the radial range from  $R_{\text{vir}}$  (as in SIM) to twice  $R_{200}$  has the effect of always reducing the  $c$ - $M$  slopes by at least 30% (twice as much as for the DM runs). In this circumstance, filaments or substructures are entering in the scene and reduce the concentration of small systems. When baryons are present the influence of the environment is more prominent for their collisional nature. The deviations from the NFW formula at large radii, in fact, are common to all three physics and are in agreement with the finding of Dolag et al. (2006) who showed that halos in a filamentary structure or in the vicinity of massive systems have an external slope that differ from an NFW and it asymptotically tends to  $-2$  instead of to  $-3$ . In addition, reducing the external radius from  $2 \times R_{200}$  to  $0.4 \times R_{200}$  produces a more significant steepening of the  $c$ - $M$  relation: the two  $\alpha$  values change by  $\sim 12\%$  for DM runs, while the difference becomes  $\sim 40$ - $45\%$  for NR and CSF  $\sim 65\%$  for AGN.

Looking with more details at the AGN case, in Figure 4, we plot the averaged density profiles of the least massive (black line) and most massive (red line) clusters normalized at  $R_{200}$ . The profiles are not exactly self similar: least massive groups are on average more concentrated than largest clusters. In the bottom panel, we show how much concentrations and NFW masses vary in relation to the external radius. Most points are lying in a precise location in this plot because the concentrations and masses of the two cases refer to the same potential well as we are modifying only the radial range of the fitting over the same mass profile. A certain degeneracy between the parameters is present. We find that our most massive systems ( $M_{\text{true}} > 10^{15} h^{-1} M_{\odot}$ ) behave exactly as in the DM simulations: their concentrations and masses vary very little with the change of the fitting radial range (the red squares in the central box show small deviations, less than 2-3%). On the other hand, the smallest systems ( $M_{\text{true}} < 1.5 \times 10^{14} h^{-1} M_{\odot}$ ) show a drop in concentration and an increase in mass when we augment the

TABLE 2

CONCENTRATION-MASS BEST-FIT PARAMETERS WITH  $1\sigma$  ERROR. THE FITTING RADIAL RANGES ARE DEFINED IN UNITS OF  $R_{200}$  (WITH  $\text{SIM}=[0.06-1.27]R_{200}$ ). THE ONLY EXCEPTION IS THE X-RAY RADIAL RANGE DEFINED BETWEEN 50 KPC AND  $0.6 \times R_{500}$ . THE BLOCK ON THE LEFT CORRESPONDS TO RESULTS OBTAINED BY FITTING THE TOTAL DENSITY PROFILE WHILE THE BLOCK ON THE RIGHT REFERS TO THE RESULTS RELATED TO THE DM ONLY DENSITY PROFILE.

	NR			DM in NR		
	N	$\alpha$	$c_0$	N	$\alpha$	$c_0$
SIM	43	$-0.158 \pm 0.038$	$3.978 \pm 0.018$	43	$-0.165 \pm 0.037$	$3.688 \pm 0.017$
X-RAY	42	$-0.159 \pm 0.041$	$4.000 \pm 0.019$	42	$-0.153 \pm 0.038$	$3.826 \pm 0.018$
[0.06–0.4]	43	$-0.174 \pm 0.041$	$4.045 \pm 0.019$	41	$-0.172 \pm 0.039$	$3.777 \pm 0.018$
[0.06–2.0]	41	$-0.119 \pm 0.035$	$4.079 \pm 0.016$	42	$-0.136 \pm 0.036$	$3.754 \pm 0.017$
[0.03–1.27]	41	$-0.132 \pm 0.038$	$4.016 \pm 0.017$	41	$-0.141 \pm 0.035$	$3.791 \pm 0.017$
[0.21–1.27]	43	$-0.139 \pm 0.039$	$3.891 \pm 0.018$	43	$-0.158 \pm 0.039$	$3.542 \pm 0.018$
	CSF			DM in CSF		
	N	$\alpha$	$c_0$	N	$\alpha$	$c_0$
SIM	40	$-0.205 \pm 0.038$	$4.781 \pm 0.017$	43	$-0.166 \pm 0.035$	$3.925 \pm 0.016$
X-RAY	–	–	–	42	$-0.129 \pm 0.033$	$4.612 \pm 0.016$
[0.06–0.4]	43	$-0.224 \pm 0.034$	$5.457 \pm 0.016$	43	$-0.167 \pm 0.036$	$4.194 \pm 0.017$
[0.06–2.0]	36	$-0.159 \pm 0.038$	$4.739 \pm 0.016$	43	$-0.137 \pm 0.032$	$3.968 \pm 0.015$
[0.03–1.27]	–	–	–	39	$-0.190 \pm 0.031$	$4.287 \pm 0.014$
[0.21–1.27]	43	$-0.154 \pm 0.038$	$4.042 \pm 0.017$	43	$-0.160 \pm 0.038$	$3.568 \pm 0.018$
	AGN			DM in AGN		
	N	$\alpha$	$c_0$	N	$\alpha$	$c_0$
SIM	43	$-0.130 \pm 0.037$	$3.856 \pm 0.017$	42	$-0.155 \pm 0.037$	$3.631 \pm 0.017$
X-RAY	37	$-0.078 \pm 0.042$	$4.891 \pm 0.020$	43	$-0.107 \pm 0.039$	$3.925 \pm 0.018$
[0.06–0.4]	43	$-0.149 \pm 0.04$	$4.072 \pm 0.019$	43	$-0.134 \pm 0.040$	$3.748 \pm 0.019$
[0.06–2.0]	41	$-0.090 \pm 0.034$	$3.943 \pm 0.015$	41	$-0.098 \pm 0.034$	$3.701 \pm 0.016$
[0.03–1.27]	24	$-0.084 \pm 0.041$	$4.113 \pm 0.019$	40	$-0.147 \pm 0.036$	$3.745 \pm 0.016$
[0.21–1.27]	43	$-0.107 \pm 0.038$	$3.641 \pm 0.018$	43	$-0.146 \pm 0.038$	$3.406 \pm 0.018$

outer radius (the black square in the central box are all consistently different from zero).

### 3.4.3. Comparison with the DM set: normalization

More generally, when we compare the  $c$ – $M$  normalizations of the hydro-simulations with the DM case, we see a consistent increase (Table 2). The CSF runs are those with the biggest deviation, especially when we reduce the external limit to  $0.4 \times R_{200}$ . This result is visualized in the top panel of Figure 5 where similarly to what shown in the lower box of Figure 4 we are reporting the variation in NFW concentrations and masses moving from the DM runs to the hydro-simulations using the SIM radial range and for  $z=0$ . The CSF simulations produced a steeper relation but also an higher normalization. Indeed, the inclusion of baryons without a strong feedback induces an increase of the concentration at all mass scale (see lower panel in the Figure). The effect is mitigated, if not completely canceled when we include the strong feedback produced by the AGNs. From the bottom panel, we can evince that the slope of AGN and NR is very similar to the DM one (both sets of green and magenta points are parallel to the DM black horizontal line). Finally, we observe that the deviations in both concentration and mass are correlated (top panel) implying that even if the simulated underlying physics is changed the potential wells of galaxy clusters are not amply modified.

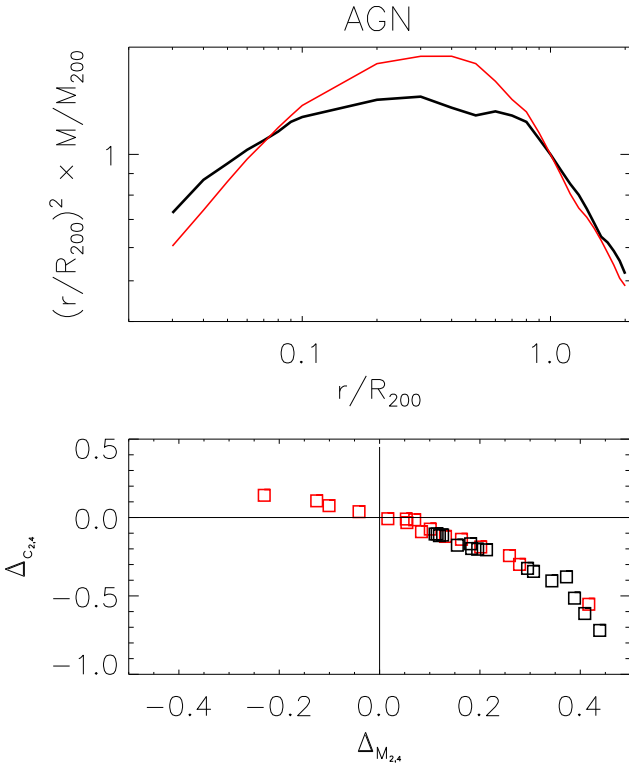


FIG. 4.— Top panel: averaged mass profiles multiplied by the radius squared of the least (black line) and most (red lines) massive clusters of the AGN sample. Bottom panel: differences between the NFW concentrations and the NFW masses:  $\Delta_{c2,4} = (c2 - c4)/c2$  and  $\Delta_{M2,4} = (M2 - M4)/M2$ , where  $c2$  ( $c4$ ) and  $M2$  ( $M4$ ) refer to values derived in the  $[0.06-2] \times R_{200}$  ( $[0.06-0.4] \times R_{200}$ ) radial range.

### 3.4.4. Comparison with previous theoretical works

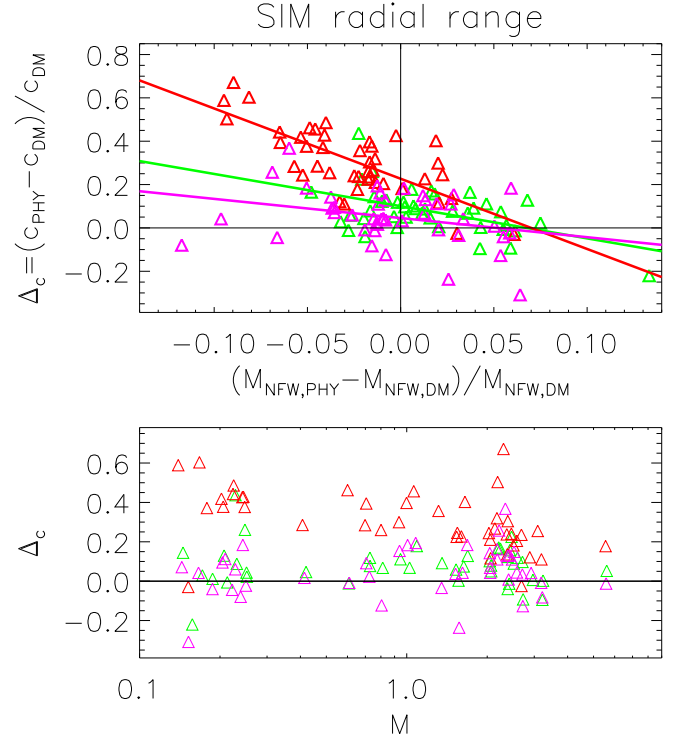


FIG. 5.— Top panel: variation in the NFW concentrations and in the masses when the quantities are computed in the hydro-simulations with respect to the DM runs. Red, green, and magenta triangles represent CSF, OVISC, and AGN results from the fitting in the SIM radial range, respectively. Bottom panel the only deviation of the concentration in function of the cluster mass.

Rudd et al. (2008), studying the influence of baryons on the matter power spectrum, analyzed how baryons affect density profiles and concentrations. Their results are very similar to ours: non radiative simulation have a concentration boosted by 5-10% while simulations with gas cooling, star formation, and SNe feedback present a larger difference (between 20 and 50%). Similar values have been found by De Boni et al. (2013) with some variations caused by the particular dark energy model considered. Duffy et al. (2010) studied, as we do, also runs with the stronger feedback by AGN. Unfortunately, they referred their studies to smaller masses, thus, a straightforward comparison cannot be done on the whole sample. However, their most-massive bin ( $M \sim 10^{14} h^{-1} M_{\odot}$ ) returns a concentration very close to their DM simulation as it is in our case.

### 3.4.5. Comparison with previous observational works

To compare with B07, SA07, and E10 we will use the re-analysis performed by Fedeli (2012) who to homogenize the results, *i*) referred to an overdensity of 200 and to the latest WMAP results Komatsu et al. (2011); *ii*) removed the relation redshift dependence, *iii*) chose a fixed pivot point at  $m_0 = 5 \times 10^{14} h^{-1} M_{\odot}$ , as we do.

We refer to all these papers for a complete description of their samples, here, we summarize the salient points:

**B07** studied 39 objects with masses from  $6 \times 10^{12} M_{\odot}$  to  $2 \times 10^{15} M_{\odot}$ . The core of their sample resides in early-type galaxies and groups (16 systems of their sample have mass below  $10^{14} M_{\odot}$ ) to which they added the massive clusters from the sample of Pointecouteau et al. (2005) and Vikhlinin et al. (2006). Restricting their analysis to only clusters with mass above  $10^{14} M_{\odot}$ ,



B07 confirmed what previously found by these latter works.

**SA07** used 34 massive halos having mass-weighted temperatures within  $R_{2500}$  above 5 keV and showing regular X-ray isoflux contours and minimal isophote centroid variations. Most of the X-ray information are contained in  $R_{2500}$  ( $\sim 0.3 \times R_{200}$ ). Finally, **E10** considered 44 very luminous nearby clusters with a minimum mass of  $10^{14} M_{\odot}$ .

In Figure 6, the CSF simulations are shown in red, NR runs in green, and AGN ones in magenta. For each physics, we chose to show the values obtained from the SIM radial ranges with thick solid lines in the case of the total density and with thin solid lines for the DM component in each physics. The vertical and horizontal lines and the black region at their intersections represent the values of the DM simulations (bold values of Table 1). Finally, the larger dotted-dashed rectangular regions indicate the location in the parameter space identified by varying the radial ranges (i.e. values between the minimum and maximum listed in Table 2).

The figure clearly confirms our findings described in the previously and summarized in the Table 2: variation in the gas physics do not lead to big changes in the slope. The highest values, registered for CSF clusters, is 40% higher than the DM slope. However, it is still much smaller than the values found by Schmidt & Allen (2007) and Ettori et al. (2010).

The normalization, instead, is affected by a larger degree. We notice that for this parameter not only the CSF clusters but also those with AGN feedback are in agreement with Buote et al. (2007) when we consider the X-ray radial range. Another agreement is between the normalization of the DM component and the value derived by Ettori et al. (2010) who also analyzed the DM component. Our agreement with E10 persists also when we compare with their normalization derived from the whole sample and after fixing the slope equal to  $\alpha = -0.1$ .

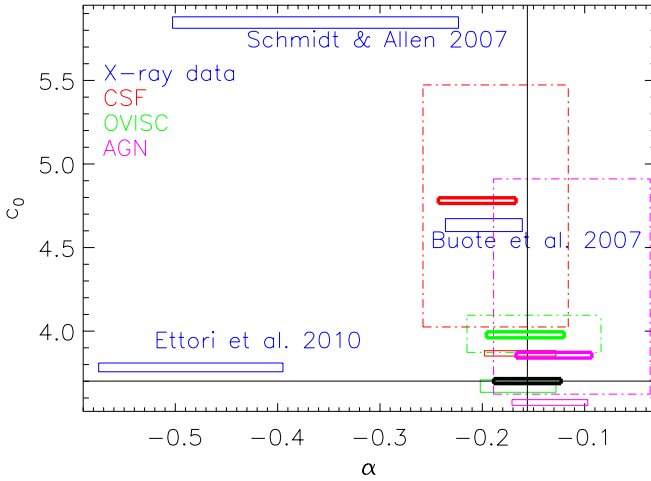


FIG. 6.— Normalization,  $c_0$ , and slope,  $\alpha$ , of the  $c-M$  relations derived in the X-ray works present in literature (in blue) and in this paper (black, green, red, and magenta represent results derived from DM, OVISC, CSF, and AGN runs, respectively). Thick and thin lines refer to the total profiles and the DM-particle profiles. Finally, the dotted-dashed lines show the regions identified in the parameter-space by varying the radial ranges (extreme values in Table 2).

To conclude this Section, we would like to point that the concentration-mass relation derived from the mass profiles of the DM particles within the hydro-simulations exhibits normalization and slope values very similar and close among them and

to those obtained from the pure N-body simulations. This result, joined with the fact that the DM profiles are always well represented by an NFW (lower panel of Fig 3) signifies that the best strategy to use in observations would be to compute the NFW concentration from the dark matter profile obtained by subtracting both the gas and stellar component from the total mass profiles. E10 pursued the same idea. They excluded the inner 50 kpc to avoid the influence of the stellar component and they further subtract the gas mass profile from the mass profile derived assuming hydrostatic equilibrium.

#### 4. OBSERVED C-M

##### 4.1. Synthetic X-ray analysis

In R12, the X-ray mass profiles have been derived following the *forward* method (Vikhlinin et al. 2006; Meneghetti et al. 2010): two fitting formulae have been adopted to fit the surface brightness and temperature profiles. The analytic best-fits have been de-projected, and the mass calculated under the assumption of spherical symmetry and hydrostatic equilibrium. We adopted the mass profiles therein derived to fit the NFW formulae using Eq. 2 and Eq. 3. In this setting, the errors on the masses are taken directly from the X-ray analysis output (typically they span from 10-12% in the most central bins to  $\sim 5\%$  close to  $R_{500}$ ).

We remind that the catalogue contains only 20 objects from the CSF sample observed at redshift  $z = 0.25$  from three different lines of sight. Therefore, even if the analysis is based on 60 X-ray images, the sample is not composed of independent systems. For this reason and because the mass range covered is limited, in the following we will stress more on biases discovery than on quantifying them thought a precise list of the parameters' values. That said, we draw attention to the fact that the characteristics of our synthetic catalogue, in number and mass range, are similar to the samples of E10 and SA07.

In Figure 7, we plot three sets of points:

- $c_i, M_i$  are the *intrinsic* parameters (black asterisks). The values are those of the 20 CSF clusters in common with the X-ray catalogue and analyzed in the previous Section using the SIM radial range at  $z = 0.25$ ;
- $c_{he}, M_{he}$  are derived from the 3D mass profiles obtained by including in the hydrostatic equilibrium equation the true 3D gas density profile and the true 3D mass-weighted temperature profile. These values are similarly obtained assuming the SIM radial range (black crosses);
- $c_X, M_X$  represent the NFW concentrations and masses obtained by fitting the X-ray hydrostatic mass profiles with an NFW formula considering the X-RAY radial range (red diamonds). However, note that the X-ray hydrostatic masses of R12 are an analytic extrapolation from 50 kpc to 15% of  $R_{500}$ . The latter value indicate the boundaries of the central excision applied in R12, choice justified by the scope of evaluating the X-ray mass bias at large radii. The  $c-M$  relation of this set of data is shown as a thin red line. The X-ray morphologically regular clusters as identified in Rasia et al. (2012a) are shown with the thick red square. The associated  $c-M$  relation is the thick red line. As found in SA07, the NFW formula is generally a good description of our X-ray data: only one system presents residual above 0.05. This is marked by a magenta square.

For direct comparison with observations, we show also the results of E10 (blue line).

Large amount of information can be read from the figure. To analyze separately the various levels of complexity involved, we will refer also to Figure 8 where we plot two sets of deviations in both concentrations and masses.

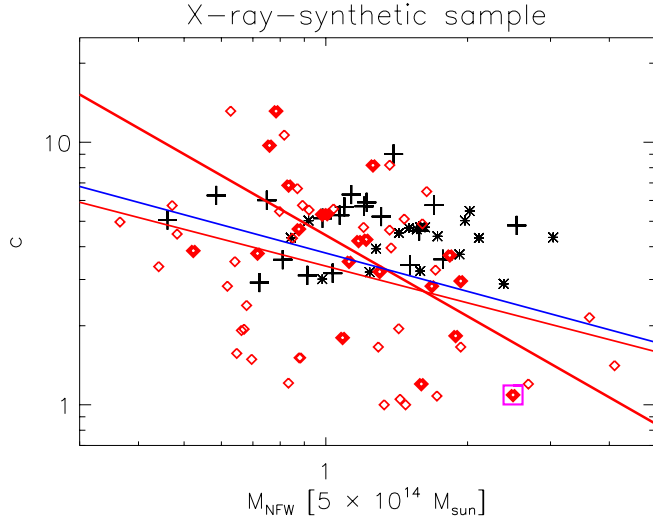


FIG. 7.— Concentration and mass values obtained from the 3D intrinsic mass profile ( $c_i, M_i$  in black asterisks), the mass profile derived by applying the hydrostatic equilibrium to the 3D gas density and 3D mass-weighted-temperature profile ( $c_{he}, M_{he}$  in black crosses), the X-ray mass profile of R12 ( $c_x, M_x$ , red diamonds). The  $c_x - M_x$  relation is shown as a red line while E10's relation is reported as a blue line. Thick diamonds and thick red line correspond to morphologically regular systems. The magenta square indicates the only X-ray cluster with a large residual value.

#### 4.1.1. Deviation caused by the hydrostatic equilibrium assumption

In the top panel of Fig. 8 we show how much concentrations and masses vary when we introduce the hydrostatic equilibrium assumption in our *intrinsic* analysis. In this case we define  $\Delta_{c(he,i)} = (c_{he} - c_i)/c_i$  and  $\Delta_{M(he,i)} = (M_{he} - M_i)/M_i$ , where  $i$  and  $he$  indicate values shown in Figure 7 by asterisks and crosses, respectively. In average, the two masses show a difference of 25%, being  $M_{he}$  lower than  $M_i$ . This value is in agreement with the results on the masses presented in R12 (red line in their Figure 6), confirming that the NFW fitting procedure is not introducing any extra bias. The concentrations show a discrepancy of 20% in the other direction without any specific correlation with either the mass of the systems,  $M_i$ , or the mass deviations,  $\Delta_{M(he,i)}$ . Consequentially, we measure a larger normalization for the concentration-mass relation  $c_{he} - M_{he}$  when we assume the hydrostatic equilibrium but we do not witness any change either in slope or in scatter (see also Lau et al. 2009).

The phenomenon emphasizes that the lack of hydrostatic equilibrium in each system increases with the radius (Rasia et al. 2004, 2006; Lau et al. 2009; Rasia et al. 2012b; Khedekar et al. 2012; Battaglia et al. 2012). The profiles of  $M_{he}$  are closer to the true mass profile at the center and diverge more in the external region, automatically producing a more concentrated profile. The effect, however, is not sensible to the mass of the object, as we deduce from the fact that the slope of the concentration-mass relation does not vary. This consideration confirms the

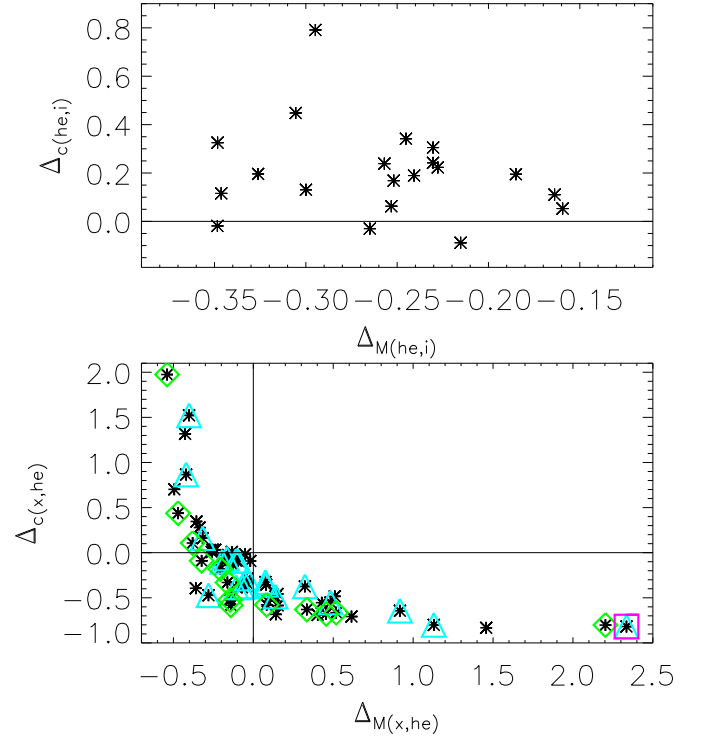


FIG. 8.— Deviation in concentrations and in masses. Top panel: we compare the values obtained from the 3D intrinsic mass profile and the mass derived assuming the hydrostatic equilibrium applied to the 3D density profile and 3D mass-weighted temperature profile. Bottom panel: these values are compared to the X-ray one where we identify also regular and disturbed systems with cyan triangles and green diamonds.

results by Piffaretti & Valdarnini (2008) who, using a more numerous sample (above 100 objects) and a larger mass range, found a negligible dependence on the mass of the hydrostatic-mass bias.

#### 4.1.2. Deviation caused by the X-ray approach

The outcomes differ when we move to compare the intrinsic hydrostatic values ( $c_{he}$  and  $M_{he}$ ) with the X-ray-derived one ( $c_x$  and  $M_x$ ). A significant increase of dispersion on both concentrations and masses is present: most clusters at high (low) mass have a lower (higher) concentration producing a clear steepening of the relation. The deviation  $\Delta_{c(x,he)} = (c_x - c_{he})/c_{he}$  and  $\Delta_{M(x,he)} = (M_x - M_{he})/M_{he}$  are shown in the bottom panel of Figure 8.

The majority of the NFW masses from the X-ray data present a further reduction, with a median value of -10%. The extra drop is caused by the temperature bias affecting this sample: the spectroscopic X-ray temperatures are lower than the mass-weighted ones because of dishomogeneity in the temperature distribution (R12).

The X-ray concentrations are significantly below the values derived from the 3D intrinsic profiles. The median deviation for the whole sample is around 35%, and show dependence on the X-ray morphology. In Figure 8, we mark with cyan triangles and green diamonds the systems belonging to the *regular* and *disturbed* class of Rasia et al. (2012a) (see Appendix of that paper for the cluster images). The average concentration deviation for the sub-sample of disturbed systems reaches 50%.

The normalization of the  $c_x - M_x$  relation is reduced with respect to both intrinsic relations. The main reason is the ex-

cision (within 15% of  $R_{500}$ ) applied in R12 to derive the X-ray masses. The cut prevents to capture the condensation of baryons in the center of the cluster similarly to the process discussed above that explains the differences in  $c_0$  when the fit is performed in the [0.2-1.27] radial range (Table 2).

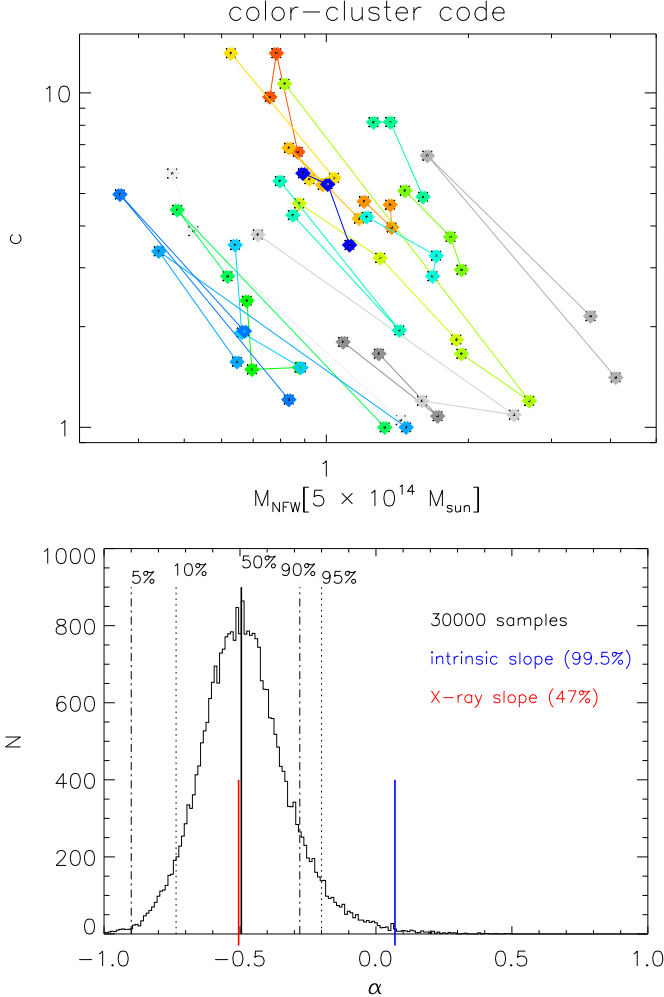


FIG. 9.— Top panel: the concentrations and the masses of the X-ray synthetic catalogue. Each color is proper of a single cluster observed in the three projections. Lower panel: Distribution of the slope of the concentration-mass-relation for 30,000 X-ray generalizations. Various percentiles of the distribution (5%, 10%, 50%, 90%, 95%) are shown by vertical lines. The thick blue line demonstrates that there is less than 3% of probability to obtain a slope equal or smaller than the intrinsic value.

#### 4.1.3. Testing degeneracy between parameters

The steepening of the relation might be a spurious effect originated from the fact that the sixty points are not completely independent, each single cluster is, instead, represented three times. Our concern is instigated by our previous results (Fig. 4 and in Fig. 5) suggesting degeneracy between NFW masses and concentrations once they are derived from the similar potential wells using slightly different procedural settings (either radial range or simulation set or, in this context, separate projections).

In the top panel of Figure 9, the set of points  $c_x$ – $M_x$  are plotted with a choice of color that helps the identification of the three projections of the same object. Clearly, this degeneracy is present. What needs to be tested is whether the direction of the

degeneracy is parallel to the relation obtained by using only one projection or it is orthogonal and, thus, steepens the relation.

To test this, we generate 30000 possible combinations of our 20 objects. In each set, a precise cluster appears only once observed from a random direction. In this fashion, we are avoiding the degeneracy caused by having ‘same-potential’ systems in the sample. This approach is more indicated than some re-sampling methods such as *bootstrap* or *jackknife* since their main assumption – independency of the 60 measurements – is definitely not satisfied in our case. For each set, we derive the concentration-mass relation. The distribution of the 30000 slopes is shown in the bottom panel of Figure 9. We overplot the 5<sup>th</sup> and 10<sup>th</sup> percentiles, the value of the intrinsic slope (black asterisks in Figure 7), and that of the X-ray catalogue (red diamonds in Figure 7).

The X-ray slope of the  $c_x$ – $M_x$  relation is exactly in the middle of the distribution meaning that the most probable slope obtained by the 20 objects is almost the same to that obtained from the enlarged sample of 60 images. From the histogram, we can evince also that there is less than 2% probability to reproduce the intrinsic slope from randomly orienting each of our clusters. This test, therefore, reassure that we are not introducing an extra bias from our sample.

#### 4.1.4. Understanding the observational-like $c$ – $M$ relation

Investigating, further, the reason for the steepening of the relation we conclude that many aspects, such as projections, dynamical status, dynamical history, hydrostatic-equilibrium mass bias, temperature bias, environment, and the dependence of the biases on the mass of the systems, are contributing at the same time without a clear driving factor.

Six extreme points are the main responsible to this feature. They are identifiable in Figure 7 by having either concentration above 10 or mass above  $2 \times 10^{15} h^{-1} M_{\odot}$  (the seventh point marked with the magenta square is not accounted to derive the relation). All the mentioned six points are related to very massive systems. The three with high concentration register a large underestimate of the hydrostatic-equilibrium masses and the NFW masses, justified by a considerable temperature bias. Since this bias increases with the radius, it leads to high concentration values. On the other hand, the three points with low concentration and high NFW mass are three massive and disturbed objects located in rich environments. They do not show major substructures but their X-ray emission remains high up to the outskirts causing a flattening of the mass profile. Note that the X-ray enhancement is present only in one of the three projections, therefore there is no intrinsic flattening of the mass profile.

Finally, even excluding these six points, the slope of  $c_x$ – $M_x$  is more than  $1\sigma$  larger than the intrinsic slope of  $c_i$ – $M_i$ . The explanation is mostly related to two factors noticed above: restricting the external radial range produces an increase in the slope and most massive systems go in both directions of reducing the concentration and increasing the mass and vice versa (red squares in the bottom panel of Fig.4).

## 5. SELECTION FUNCTION

Selecting the sample according the X-ray luminosity has been recognized as a source of bias in X-ray scaling relations (e.g. Nord et al. 2008; Pratt et al. 2009). The wide scatter in the luminosity-mass relation induces a concomitant presence of a broad range of masses, especially, when small systems are included (Pratt et al. 2009; Stanek et al. 2010; Mantz et al. 2010;

Allen et al. 2011). The correspondence between the theoretical selection – based on mass – and the observational one – based on the X-ray emission – is, therefore, compromised.

At the same time, also the concentration-mass relation presents a significant dispersion: galactic or small groups masses can have a concentration that vary even by an order of magnitude (e.g. Rudd et al. 2008; Ludlow et al. 2012; Bahé et al. 2012; De Boni et al. 2013).

Using the X-ray catalogue we investigate how the two large scatters combine together and what is the impact of choosing the cluster on the basis of their X-ray luminosity, temperature, and SZ-signal instead of their mass. We create various subsamples selecting systems with:

- true mass higher than  $M_{\text{true}} > 10^{15} h^{-1} M_{\odot}$  (subsample  $M_{\text{high}}$ ) and higher than  $M_{\text{true}} > 7 \times 10^{14} h^{-1} M_{\odot}$  ( $M_{\text{med}}$ );
- X-ray luminosity higher than  $L_X > 14 \times 10^{44}$  erg/s ( $L_{\text{high}}$ ) and higher than  $L > 7 \times 10^{44}$  erg/s ( $L_{\text{med}}$ );
- SZ-signal higher than  $SZ > 60$  ( $SZ_{\text{high}}$ ) and higher than  $SZ > 40$  ( $SZ_{\text{med}}$ );
- mass-weighted temperature higher than  $T_{\text{MW}} > 6$  keV ( $T_{\text{high}}$ ) and  $T_{\text{MW}} > 4$  keV ( $T_{\text{med}}$ ).

The subsamples denoted with the subscript ‘high’ account for either 15 or 18 points, while the ‘med’ compilations include  $35 \div 42$  points. The mass definition used in this context is based on the true 3D mass computed within  $R_{200}$  while the observable quantities are measured as projected quantities and integrated across the whole field of view. The Compton Y parameter called ‘SZ’ is the integral over the whole field of view of adimensional quantity  $dI/I$ .

For each sub-sample we recompute the  $c-M$  relation and compare the derived slopes. In Figure 10, we color-code the different cuts in flux/luminosity as example. Selecting the clusters by way of their luminosity (subsamples  $L_{\text{high}}$  or  $L_{\text{med}}$ ) convey the most divergent result with respect to the mass cuts (subsamples  $M_{\text{high}}$  and  $M_{\text{med}}$ , respectively).

The  $L_{\text{high}}$  clusters show a slope twice as steep as the slope of the systems in the  $M_{\text{high}}$  subsample and 3 times steeper than the entire set of objects. Among the smallest clusters, those that emit the most have higher concentration. Consequently, a flux-limited sample will tend to produce an artificial increase of the slope.

This theoretical finding can be easily translated to an observational interpretation: at fixed mass the objects that are more X-ray luminous tend to be the morphologically-regular cool-core clusters who exhibit a larger concentrations than non cool core objects. The X-ray surface-brightness concentration was, indeed, the method followed by Santos et al. (2008) to identify cool-core systems at high redshift. The bias toward cool-core systems for X-ray cluster sample was also studied in details by Eckert et al. (2011).

When the objects are selected via their mass-weighted temperature, we see a good agreement with the  $c-M$  relation of the mass-selected objects, as expected from the relative small scatter in the relation  $T_{\text{MW}} - M$ . The SZ-selection instead shows a slight increase of  $\sim 15\%$  of the slopes for both  $SZ_{\text{high}}$  and  $SZ_{\text{med}}$  subsamples with respect to  $M_{\text{high}}$  and  $M_{\text{med}}$  subsamples. This difference is, however, not worrisome being within  $1 \sigma$ . Concluding our results are suggesting that the SZ selection is more similar to the mass (or theoretical) selection, while a compilation based on the X-ray luminosity substantially contaminate the result in the direction of increasing the slope.

The findings derived from our synthetic catalogue might ex-

plain the differences among the various observational concentration-mass relations. While E10 and SA07, with  $c-M$ ’s slope around  $-0.5$ , are based on very luminous clusters, the samples of B07 and Host & Hansen (2011), with slopes closer to the theoretical one, involve also early-type galaxies and small groups that *were not selected* for their X-ray power. The normalization spread among these works is also in agreement with our findings about the differences caused by the change of the radial range: SA07 limited the information to very central regions while all the other works extended beyond  $R_{2500}$ .

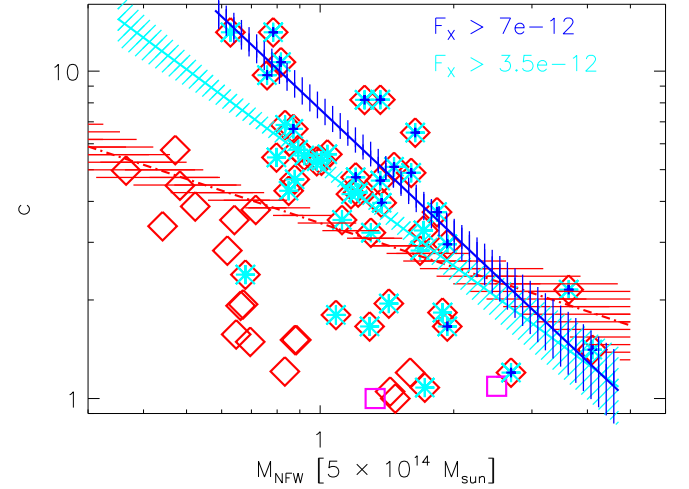


FIG. 10.— The concentration-mass for the X-ray synthetic catalogue binned by the flux emission in units of erg/s. In blue all clusters with X-ray flux (luminosity) above  $7 \times 10^{-12}$  erg/s ( $14 \times 10^{44}$  erg/s), in cyan those with flux above  $3.5 \times 10^{-12}$  erg/s ( $7 \times 10^{44}$  erg/s), in red all the clusters with an acceptable NFW fit. With the same colors, we also plot the best-fit scaling relations as solid line and its  $1\text{-sigma}$  variation as shaded region. The magenta squares in the bottom of the figure refer to the objects with large NFW residual and not used in the  $c-M$  relation fitting.

## 6. CONCLUSIONS

Recent claims about the discrepancy between the observed and simulated  $c-M$  relation were declared real. Here, we tested if the difference is instead induced by the two approaches followed to derive the values of concentration and NFW masses. Specifically, we checked at the influence of *i*) the radial range adopted to perform the NFW fit of the mass profile, *ii*) the baryonic-physics models included in the simulation, *iii*) the proper X-ray description, and *iv*) the impact of the selection function. To accomplish the first two tasks we analyzed four sets of 52 clusters simulated four times varying the description of the ICM physics. The latter two aspects were, instead, addressed by studying the synthetic catalogue of the 60 *Chandra*-like X-ray images (R12). The four sets of physics considered include dark matter (DM), no-radiative runs (OVISC), cooling, star formation and feedback by SN (CSF), and cooling, star formation, and feedback from AGN (AGN).

- **Radial range.** Using the DM set we registered an increase in both slope and normalization of the  $c-M$  relation when the most external radius considered during the NFW fitting is reduced from  $2 \times R_{200}$  to  $0.4 \times R_{200}$ . Extending the fit to inner regions, instead, produces an higher normalization accompanied by a shallower slope. All these differences, even if robust (inter-



mediate choices of either internal or external radius reproduce the same trend of changes in slopes and normalizations), are mild,  $\Delta\alpha \sim 10-20\%$  and  $\Delta c_0 \sim 3-5\%$ , due to the large scatter of the points. They, however, become more pronounced once baryons are introduced ( $\alpha$  and  $c_0$  increases up to 60% and 15%, respectively).

- **NFW fitting and hydro-simulations.** The total mass profiles of the radiative simulations (CSF and AGN) show large residuals in the innermost region. The cause is the efficient condensation of baryons in form of stellar component that drastically steepens the total density profile. The NR clusters at  $z=0$  are, instead, well described by the NFW formula. For all physics and radial ranges, the results related to the DM component are always robustly similar.
- **Baryon physics.** The relations derived from simulations with baryons have always a larger normalization than those from the DM halos. The phenomenon of adiabatic contraction is further aggravated in case of radiative simulations. Studying the influence of the radial range on hydro-simulations we noticed that smaller objects are more affected by the change of either internal or external radius. The CSF set is characterized by a steeper and higher  $c-M$  relation (increases around 30% in both normalization and slope with respect to the DM results in the SIM radial range). Both effects are strongly reduced when AGNs are included as source of feedback. In this case, the slopes are much closer to the DM values, with variation of order of few percent. Within  $<10\%$  is also the difference measured from the NR set. Comparing the results of our intrinsic analysis with the observational ones we found that only the CSF slope overlaps with the values found in Buote et al. (2007). Even in this case, however, it does not reproduce the observations by Schmidt & Allen (2007); Ettori et al. (2010).
- **X-ray  $c-M$ .** While the change of the radial range and the baryonic physics contribute only minimally to explain the gap between the theoretical and observed  $c-M$  slope, the analysis performed on our X-ray catalogue gave more insights. The hydrostatic-equilibrium assumption introduces a general reduction of the NFW masses (25%) and an increase of the concentrations (20%). The first result is explained by the HE mass bias. Its radial dependence justifies the second finding. The NFW masses and concentration derived from the X-ray synthetic catalogue have a huge dispersion with respect to the intrinsic results. Most points show an increase (decrease) of concentration at small (large) masses. The slope derived from our X-ray sample is in agreement with Ettori et al. (2010) and is not influenced by the construction of our sample. The relation steepening is caused by the concomitant presence of multiple effects such as projections, environment, dynamical state, dynamical history, mass bias, temperature bias, and their dependences on the radius and on the mass of the system. Our morphologically regular objects show a slope 50% steeper than the entire sample. This might seem in contrast with the finding of E10 who reported a 20-30% shallower relation for their most relaxed systems. However, the selection of the two subsamples is based on

different conditions: in our case regular systems have smaller third order power ratio and centroid shift while in E10 relaxed objects were defined as having lower central entropy level.

- **Selection function** By comparing the  $c-M$  relations of various subsamples defined on the basis of X-ray luminosity, mass-weighted temperature, SZ signal, and mass we verified the influence of the selection function. The clusters selected via the mass-weighted temperature or the SZ-signal return similar results than those derived from the mass-selected samples. The situation is quite different when we choose the systems via their X-ray luminosity. The  $c-M$  slope of the fifteen brightest objects is twice as steep as the relation from the fifteen most massive clusters. At fixed mass, more luminous clusters have systematically higher concentrations.

Numerical works present in literature are based on many hundreds of halos. The effects of environment, dynamical status, and presence of substructures statistically cancel out when such large set of objects is considered. This is not the case when few tens of objects are selected as done in observational works. The comparison between the two samples, therefore, cannot be as straightforward. From our analysis of the intrinsic profile, it emerged that smaller objects are more strongly affected by the choice of the radial range, and their mass profiles are more easily distorted by the mentioned effects. Furthermore, if groups or early-type elliptical are chosen for their X-ray power, luckily, they will not represent the entire population of similar-mass objects but they will mostly be characterized by higher concentrations.

## APPENDIX

In the Table 3 we report the normalizations and slopes of the  $c-M$  relations derived in the four sets of simulations at  $z=0.25$  adopting all the radial ranges presented above. The DM profiles within the hydro-simulation behave very similarly to the profiles from the DM set, therefore, we choose to not list them. The significant radii  $R_{500}$  and  $R_{200}$  are recomputed at  $z=0.25$ . Comparing the normalizations of the SIM radial range at  $z=0.25$  with those at  $z=0$ , we notice that they are related to each other through:  $c_0(z=0) = c_0(z=0.25) \times (1+z)^{0.4}$ .

**Acknowledgment.** ER thanks Cosimo Fedeli for sharing his results on the concentration-mass relation and for discussions at the early stage of this project. We thank Volker Springel for providing us with the GADGET-3 code. Simulations have been carried out at the CINECA supercomputing Centre in Bologna, with CPU time assigned through ISCRA proposals and through an agreement with University of Trieste. We acknowledge financial support by the following grants: National Science Foundation AST-1210973, SAO TM3-14008X (issued under NASA Contract Number NAS8-03060), ASI-INAF I/023/05/0 and I/088/06/0, Marie Curie Initial Training Network CosmoComp (PITN-GA-2009-238356) funded within the European Commission's Framework Programme 7, PRIN-INAF09 project "Towards an Italian Network for Computational Cosmology", PRIN-MIUR09 "Tracing the growth of structures in the Universe", and INFN PD51. ER and MM would like to thank the Michigan Center for Theoretical Physics for supporting the collaboration.



TABLE 3

CONCENTRATION-MASS BEST-FIT PARAMETERS WITH  $1\sigma$  ERROR. THE FITTING RADIAL RANGES ARE DEFINED IN UNITS OF  $R_{200}$  (WITH  $\text{SIM}=[0.06-1.27]R_{200}$ ) WITH THE ONLY EXCEPTION OF THE X-RAY RADIAL RANGE DEFINED BETWEEN 50 KPC AND  $0.6 \times R_{500}$ .

		N	$\alpha$	$c_0$
DM	SIM	39	$-0.076 \pm 0.045$	$3.395 \pm 0.019$
	X-RAY	43	$-0.098 \pm 0.039$	$3.679 \pm 0.020$
	[0.06–0.4]	40	$-0.109 \pm 0.044$	$3.551 \pm 0.021$
	[0.06–2.0]	40	$-0.058 \pm 0.045$	$3.338 \pm 0.019$
	[0.03–1.27]	38	$-0.073 \pm 0.043$	$3.542 \pm 0.019$
NR	SIM	35	$-0.067 \pm 0.051$	$3.609 \pm 0.019$
	X-RAY	–	–	–
	[0.06–0.4]	36	$-0.116 \pm 0.049$	$3.735 \pm 0.019$
	[0.06–2.0]	35	$-0.049 \pm 0.047$	$3.625 \pm 0.017$
	[0.03–1.27]	33	$-0.055 \pm 0.049$	$3.600 \pm 0.018$
CSF	SIM	33	$-0.09 \pm 0.052$	$4.397 \pm 0.020$
	X-RAY	–	–	–
	[0.06–0.4]	39	$-0.175 \pm 0.039$	$5.218 \pm 0.019$
	[0.06–2.0]	32	$-0.073 \pm 0.051$	$4.304 \pm 0.019$
	[0.03–1.27]	–	–	–
AGN	SIM	40	$-0.087 \pm 0.045$	$3.576 \pm 0.020$
	X-RAY	37	$-0.107 \pm 0.042$	$4.891 \pm 0.020$
	[0.06–0.4]	40	$-0.132 \pm 0.044$	$3.872 \pm 0.021$
	[0.06–2.0]	39	$-0.056 \pm 0.044$	$3.551 \pm 0.018$
	[0.03–1.27]	36	$-0.041 \pm 0.043$	$3.832 \pm 0.018$
	[0.21–1.27]	40	$-0.031 \pm 0.051$	$3.233 \pm 0.022$

## REFERENCES

- Abadi, M. G., Navarro, J. F., Pardo, M., Babul, A., & Steinmetz, M. 2010, *MNRAS*, 407, 435
- Allen, S. W., Evrard, A. E., & Mantz, A. B. 2011, *ARA&A*, 49, 409
- Anders, E. & Grevesse, N. 1989, *Geochimica et Cosmochimica Acta*, 53, 197
- Bahé, Y. M., McCarthy, I. G., & King, L. J. 2012, *MNRAS*, 421, 1073
- Balaguera-Antolinez, A. & Porciani, C. 2012, *ArXiv*: 1210.4117
- Baldi, M. 2012, *Physics of the Dark Universe*, 1, 162
- Barnes, J. & White, S. D. M. 1984, *MNRAS*, 211, 753
- Battaglia, N., Bond, J. R., Pfrommer, C., & Sievers, J. L. 2012, *ArXiv*: 1209.4082
- Bhattacharya, S., Habib, S., & Heitmann, K. 2011, *ArXiv*: 1112.5479
- Blumenthal, G. R., Faber, S. M., Flores, R., & Primack, J. R. 1986, *ApJ*, 301, 27
- Bonafede, A., Dolag, K., Stasyszyn, F., Murante, G., & Borgani, S. 2011, *MNRAS*, 418, 2234
- Borgani, S. & Kravtsov, A. 2011, *Advanced Science Letters*, 4, 204
- Bullock, J. S., Kolatt, T. S., Sigad, Y., Somerville, R. S., Kravtsov, A. V., Klypin, A. A., Primack, J. R., & Dekel, A. 2001, *MNRAS*, 321, 559
- Buote, D. A., Gastaldello, F., Humphrey, P. J., Zappacosta, L., Bullock, J. S., Brighenti, F., & Mathews, W. G. 2007, *ApJ*, 664, 123
- Chabrier, G. 2003, *PASP*, 115, 763
- Cui, W., Borgani, S., Dolag, K., Murante, G., & Tornatore, L. 2012, *MNRAS*, 423, 2279
- Dalal, N., Lithwick, Y., & Kuhlen, M. 2010, *ArXiv*: 1010.2539
- De Boni, C., Ettori, S., Dolag, K., & Moscardini, L. 2013, *MNRAS*, 428, 2921
- Dolag, K., Bartelmann, M., Perrotta, F., Baccigalupi, C., Moscardini, L., Meneghetti, M., & Tormen, G. 2004, *A&A*, 416, 853
- Dolag, K., Borgani, S., Murante, G., & Springel, V. 2009, *MNRAS*, 399, 497
- Dolag, K., Meneghetti, M., Moscardini, L., Rasia, E., & Bonaldi, A. 2006, *MNRAS*, 370, 656
- Duffy, A. R., Schaye, J., Kay, S. T., & Dalla Vecchia, C. 2008, *MNRAS*, 390, L64
- Duffy, A. R., Schaye, J., Kay, S. T., Dalla Vecchia, C., Battye, R. A., & Booth, C. M. 2010, *MNRAS*, 405, 2161
- Eckert, D., Molendi, S., & Paltani, S. 2011, *A&A*, 526, A79
- Eke, V. R., Navarro, J. F., & Steinmetz, M. 2001, *ApJ*, 554, 114
- Ettori, S., Gastaldello, F., Leccardi, A., Molendi, S., Rossetti, M., Buote, D., & Meneghetti, M. 2010, *A&A*, 524, 68
- Fabjan, D., Borgani, S., Tornatore, L., Saro, A., Murante, G., & Dolag, K. 2010, *MNRAS*, 401, 1670
- Fedeli, C. 2012, *MNRAS*, 424, 1244
- Ferland, G. J., Korista, K. T., Verner, D. A., Ferguson, J. W., Kingdon, J. B., & Verner, E. M. 1998, *PASP*, 110, 761
- Gao, L., Navarro, J. F., Cole, S., Frenk, C. S., White, S. D. M., Springel, V., Jenkins, A., & Neto, A. F. 2008, *MNRAS*, 387, 536
- Gardini, A., Rasia, E., Mazzotta, P., Tormen, G., De Grandi, S., & Moscardini, L. 2004, *MNRAS*, 351, 505
- Gastaldello, F., Buote, D. A., Humphrey, P. J., Zappacosta, L., Bullock, J. S., Brighenti, F., & Mathews, W. G. 2007, *ApJ*, 669, 158
- Gnedin, O. Y., Ceverino, D., Gnedin, N. Y., Klypin, A. A., Kravtsov, A. V., Levine, R., Nagai, D., & Yepes, G. 2011, *ArXiv*: 1108.5736
- Gnedin, O. Y., Kravtsov, A. V., Klypin, A. A., & Nagai, D. 2004, *ApJ*, 616, 16
- Governato, F., Zolotov, A., Pontzen, A., Christensen, C., Oh, S. H., Brooks, A. M., Quinn, T., Shen, S., & Wadsley, J. 2012, *MNRAS*, 422, 1231
- Grossi, M. & Springel, V. 2009, *MNRAS*, 394, 1559
- Gustafsson, M., Fairbairn, M., & Sommer-Larsen, J. 2006, *Physical Review D*, 74, 123522
- Haardt, F. & Madau, P. 2001, in *Clusters of Galaxies and the High Redshift Universe Observed in X-rays*, ed. D. M. Neumann & J. T. V. Tran
- Host, O. & Hansen, S. H. 2011, *ApJ*, 736, 52
- Hu, W. & Kravtsov, A. V. 2003, *ApJ*, 584, 702
- Khedekar, S., Churazov, E., Kravtsov, A., Zhuravleva, I., Lau, E. T., Nagai, D., & Sunyaev, R. 2012, *ArXiv*: 1211.3358
- Killedar, M., Borgani, S., Meneghetti, M., Dolag, K., Fabjan, D., & Tornatore, L. 2012, *MNRAS*, 427, 533
- Komatsu, E., Smith, K. M., Dunkley, J., Bennett, C. L., Gold, B., Hinshaw, G., Jarosik, N., Larson, D., Nolte, M. R., Page, L., Spergel, D. N., Halpern, M., Hill, R. S., Kogut, A., Limon, M., Meyer, S. S., Odegard, N., Tucker, G. S., Weiland, J. L., Wollack, E., & Wright, E. L. 2011, *ApJS*, 192, 18
- Kravtsov, A. V. & Borgani, S. 2012, *ARA&A*, 50, 353
- Kwan, J., Bhattacharya, S., Heitmann, K., & Habib, S. 2012, *ArXiv*: 1210.1576
- Lau, E. T., Kravtsov, A. V., & Nagai, D. 2009, *ApJ*, 705, 1129
- Lau, E. T., Nagai, D., Kravtsov, A. V., & Zentner, A. R. 2011, *ApJ*, 734, 93
- Ludlow, A. D., Navarro, J. F., Li, M., Angulo, R. E., Boylan-Kolchin, M., & Bett, P. E. 2012, *ArXiv e-prints*
- Macciò, A. V., Stinson, G., Brook, C. B., Wadsley, J., Couchman, H. M. P., Shen, S., Gibson, B. K., & Quinn, T. 2012, *ApJL*, 744, L9
- Mantz, A., Allen, S. W., Ebeling, H., Rapetti, D., & Drlica-Wagner, A. 2010, *MNRAS*, 406, 1773
- Martizzi, D., Teyssier, R., & Moore, B. 2012, *ArXiv e-prints*
- Meneghetti, M., Rasia, E., Merten, J., Bellagamba, F., Ettori, S., Mazzotta, P., Dolag, K., & Marri, S. 2010, *A&A*, 514, A93

- Navarro, J. F., Frenk, C. S., & White, S. D. M. 1996, *ApJ*, 462, 563
- Navarro, J. F., Frenk, C. S., & White, S. D. M. 1997, *ApJ*, 490, 493
- Neto, A. F., Gao, L., Bett, P., Cole, S., Navarro, J. F., Frenk, C. S., White, S. D. M., Springel, V., & Jenkins, A. 2007, *MNRAS*, 381, 1450
- Nord, B., Stanek, R., Rasia, E., & Evrard, A. E. 2008, *MNRAS*, 383, L10
- Ogiya, G. & Mori, M. 2011, *ApJL*, 736, L2
- Padovani, P. & Matteucci, F. 1993, *ApJ*, 416, 26
- Pedrosa, S., Tissera, P. B., & Scannapieco, C. 2009, *MNRAS*, 395, L57
- Piffaretti, R. & Valdarnini, R. 2008, *A&A*, 491, 71
- Pointecouteau, E., Arnaud, M., & Pratt, G. W. 2005, *A&A*, 435, 1
- Power, C., Navarro, J. F., Jenkins, A., Frenk, C. S., White, S. D. M., Springel, V., Stadel, J., & Quinn, T. 2003, *MNRAS*, 338, 14
- Pratt, G. W. & Arnaud, M. 2005, *A&A*, 429, 791
- Pratt, G. W., Croston, J. H., Arnaud, M., & Böhringer, H. 2009, *A&A*, 498, 361
- Ragone-Figueroa, C., Granato, G. L., & Abadi, M. G. 2012, *MNRAS*, 423, 3243
- Rasia, E., Ettori, S., Moscardini, L., Mazzotta, P., Borgani, S., Dolag, K., Tormen, G., Cheng, L. M., & Diaferio, A. 2006, *MNRAS*, 369, 2013
- Rasia, E., Mazzotta, P., Bourdin, H., Borgani, S., Tornatore, L., Ettori, S., Dolag, K., & Moscardini, L. 2008, *ApJ*, 674, 728
- Rasia, E., Meneghetti, M., & Ettori, S. 2012a, *ArXiv:1211.7040*
- Rasia, E., Meneghetti, M., Martino, R., Borgani, S., Bonafede, A., Dolag, K., Ettori, S., Fabjan, D., Giocoli, C., Mazzotta, P., Merten, J., Radovich, M., & Tornatore, L. 2012b, *New Journal of Physics*, 14, 055018
- Rasia, E., Tormen, G., & Moscardini, L. 2004, *MNRAS*, 351, 237
- Rudd, D. H., Zentner, A. R., & Kravtsov, A. V. 2008, *ApJ*, 672, 19
- Ryden, B. S. & Gunn, J. E. 1987, *ApJ*, 318, 15
- Santos, J. S., Rosati, P., Tozzi, P., Böhringer, H., Ettori, S., & Bignamini, A. 2008, *A&A*, 483, 35
- Schmidt, R. W. & Allen, S. W. 2007, *MNRAS*, 379, 209
- Sijacki, D., Springel, V., Di Matteo, T., & Hernquist, L. 2007, *MNRAS*, 380, 877
- Springel, V. 2005, *MNRAS*, 364, 1105
- Springel, V., Di Matteo, T., & Hernquist, L. 2005, *MNRAS*, 361, 776
- Springel, V. & Hernquist, L. 2003, *MNRAS*, 339, 289
- Stanek, R., Rasia, E., Evrard, A. E., Pearce, F., & Gazzola, L. 2010, *ApJ*, 715, 1508
- Stanek, R., Rudd, D., & Evrard, A. E. 2009, *MNRAS*, 394, L11
- Teyssier, R., Pontzen, A., Dubois, Y., & Read, J. I. 2013, *MNRAS*, 493
- Tissera, P. B., White, S. D. M., Pedrosa, S., & Scannapieco, C. 2010, *MNRAS*, 406, 922
- Tormen, G., Bouchet, F., & White, S. D. M. 1997, *MNRAS*, 286, 865
- Tornatore, L., Borgani, S., Dolag, K., & Matteucci, F. 2007, *MNRAS*, 382, 1050
- van Daalen, M. P., Schaye, J., Booth, C. M., & Dalla Vecchia, C. 2011, *MNRAS*, 415, 3649
- Vikhlinin, A., Kravtsov, A., Forman, W., Jones, C., Markevitch, M., Murray, S. S., & Van Speybroeck, L. 2006, *ApJ*, 640, 691
- Voit, G. M. 2005, *Reviews of Modern Physics*, 77, 207
- Wiersma, R. P. C., Schaye, J., & Smith, B. D. 2009, *MNRAS*, 393, 99
- Zemp, M., Gnedin, O. Y., Gnedin, N. Y., & Kravtsov, A. V. 2012, *ApJ*, 748, 54
- Zhao, D. H., Jing, Y. P., Mo, H. J., & Börner, G. 2009, *ApJ*, 707, 354
- Zhu, X.-J. & Pan, J. 2012, *Research in Astronomy and Astrophysics*, 12, 2